nature communications

Article

https://doi.org/10.1038/s41467-025-59457-z

Spatiotemporal deciphering of dynamic the FUS interactome during liquid-liquid phase separation in living cells

Received: 28 March 2024

Accepted: 22 April 2025

Published online: 09 May 2025

Check for updates

Sunfengda Song[1,2], Haiyang Xie[1,2], Qingwen Wang[1,2], Xinyi Sun[1,2], Jiasu Xu[1,2], Rui Chen[1,2], Yuankang Zhu[1], Lai Jiang[1] & Xianting Ding[1,2]

Liquid-liquid phase separations (LLPS) are membraneless organelles driven by biomolecule assembly and are implicated in cellular physiological activities. However, spatiotemporal deciphering of the dynamic proteome in living cells during LLPS formation remains challenging. Here, we introduce the **C**omposition of **L**LPS proteome **A**ssembly by **P**roximity labeling-assisted **M**ass spectrometry (CLAPM). We demonstrate that CLAPM can instantaneously label and monitor the FUS interactome shifts within intracellular droplets undergoing spatiotemporal LLPS. We report 129, 182 and 822 proteins specifically present in the LLPS droplets of HeLa, HEK 293 T and neuronal cells respectively. CLAPM further categorizes spatiotemporal dynamic proteome in droplets for living neuronal cells and identifies 596 LLPS-aboriginal proteins, 226 LLPS-dependent proteins and 58 LLPS-sensitive proteins. For validation, we uncover 11 previously unknown LLPS proteins in vivo. CLAPM provides a versatile tool to decipher proteins involved in LLPS and enables the accurate characterization of dynamic proteome in living cells.

Liquid-liquid phase separations (LLPS) lead to membraneless organelle that modulates various biological processes, including innate immunity[1,2], gene transcription regulation[3], heterochromatin formation[4,5], stress granule assembly[6], autophagy[7,8], neural signal transmission[9], cancer, and neurodegenerative diseases[10–13]. Multivalent interactions between nucleic acids and proteins drive the assembly of LLPS droplets, which orchestrate complex and elusive cellular dynamics[14,15]. Proteomic information and co-aggregation of proteins within LLPS droplets are crucial for proteins' biological functions[16–20]. For example, the alterations in the types and quantities of proteins within the droplets lead to pathological protein aggregation, which is closely associated with neurodegenerative diseases[21–25]. Uncontrolled aggregation of phase-separated proteins is a hallmark of neurodegenerative diseases, including amyotrophic lateral sclerosis (ALS) and frontotemporal dementia (FTD)[12,24–26]. In the majority of ALS cases, aggregates of an RNA-binding protein (RBP), namely TDP-43, have been observed[23]. Mutations in other RBPs, including fused in sarcoma protein (FUS) and hnRNPA1/A2, have been reported in familial neurodegenerative patients[8,10,24]. Thus, identifying aberrantly aggregated proteins in LLPS droplets could give a deeper insight into gene regulation and phenotype in human health and disease.

The analysis of weak (or low-affinity), transient, and dynamic protein-protein interactions occurring within LLPS droplets has been a long-standing challenge due to the inherent instability of LLPS droplets[27]. Currently, several in vitro protein purification methods have been employed to mimic LLPS and examine the protein content within droplets[28,29]. However, in vitro simulation methods may only partially replicate the LLPS environment inside living cells, which often suffer from potential content loss and false-positive results. The protein composition within droplets is also influenced by cell type, properties of LLPS core proteins, and disease-associated mutations. Although in vivo fluorescent labeling methods have also being

[1]Department of Anesthesiology and Surgical Intensive Care Unit, Xinhua Hospital, School of Medicine and School of Biomedical Engineering, Shanghai Jiao Tong University, Shanghai, China. [2]State Key Laboratory of Oncogenes and Related Genes, Institute for Personalized Medicine, Shanghai Jiao Tong University, Shanghai, China. e-mail: dingxianting@sjtu.edu.cn

reported to analyze the composition of LLPS droplets, they can only label a few proteins, and hardly grasp the complex proteomics network involved in LLPS droplets[26,30–32].

In recent years, several intracellular labeling methods have been reported for mapping molecular interactions and subcellular localization in living cells. The proximity labeling (PL) technique uses peroxidases to label proteins within a nanoscale neighborhood[33–36]. BioID is a commonly used enzyme, but may result in long labeling time and cellular toxicity to substrates. The spatiotemporal unpredictability of LLPS and the diffused labeling during protein translation remain unresolved. The feasibility and capability of dynamically analyzing the proteome composition of LLPS droplets have not been addressed. Markmiller et al. used proximity labeling to study the G3BP1 interactome in stress granules[36]. However, analysis of the dynamics of the interactome in FUS-mediated LLPS droplets is still missing, especially under pathological mutations.

Here, we demonstrated the Composition of LLPS proteome Assembly by Proximity labeling assisted Mass spectrometry (CLAPM) strategy, which permits in vivo PL and allows for spatiotemporal analysis of proteomics within the LLPS droplets (Fig. 1a). In contrast to traditional PL enzymes, CLAPM adopted ascorbate peroxidase (APEX2), which offers high efficiency and low substrate toxicity, making it a desirable enzyme for PL reactions. In addition, CLAPM utilized chemical labeling rather than photo-click chemistry, that labels interacting proteins under ultraviolet (UV) irradiation. Therefore, during photochemical reactions, CLAPM avoids the false positives on mass spectrometry generated by reactive species (such as nitrenes, carbenes, and radicals). Thus, CLAPM provides spatiotemporal controllability and accuracy in living cells and captures weak and transient protein assembly within LLPS droplets, including previously unknown LLPS proteins. Moreover, unlike the conventional fluorescence labeling methods that are limited by the fixed number of fluorescent tags, CLAPM enables simultaneous labeling of the entire FUS interactome within the droplets.

We constructed a FUS-mediated LLPS model in living cells. With CLAPM, we uncovered three dynamic protein groups during LLPS formation in living neuronal cells, namely LLPS-aboriginal, LLPS-dependent, and LLPS-sensitive proteins. We demonstrated these three protein groups formed distinct, densely interconnected protein-protein interaction networks (PINs) that rapidly assembled and disassembled under LLPS conditions. We compared the FUS interactome composition of LLPS droplets obtained from our results with the public LLPS dataset and identified 65% additional previously unknown protein coverage. We found that the FUS interactome exhibits a high content of disordered domains and low repetitive domains. Furthermore, we found the aberrant protein composition, such as CDC20, FDXP1, DMX2, EIF4B, and SF3B5, within the LLPS droplets mediated by FUS in pathological neuronal cells was closely associated with neurodegenerative diseases. We further validated 11 previously unreported LLPS aberrant protein expressions in brain samples from APP/PS1 mice as compared to the wild-type mice. CLAPM offers a general method to decipher proteins involved in LLPS assembly and enables the accurate characterization of the dynamic FUS interactome in living cells.

Results

Design of CLAPM for spatiotemporal proteome profiling in LLPS droplets

The FUS protein is crucial for LLPS formation and is firmly localized within LLPS droplets[10,24,37,38]. FUS is closely associated with neurodegenerative diseases. APEX2 has been shown to efficiently biotinylate neighboring proteins in the presence of biotin phenol (BP) and hydrogen peroxide (H_2O_2) within 1 min (Fig.1a)[39]. We designed a recombinant plasmid to stably express the FUS-APEX2-EGFP fusion protein in target cells. APEX2-EGFP plasmid was constructed as a control. Upon treatment of the cells with sodium arsenite, intracellular LLPS droplets formed under external stimuli. We simultaneously performed PL and used magnetic bead enrichment to harvest biotinylated proteins. (Fig. 1b). We used an Orbitrap liquid chromatography-mass spectrometry system (LC-MS) to identify biotinylated proteins. For control groups, the above procedure was conducted in the absence of PL substrate, sodium arsenite stimulation, or FUS protein. Through statistical analysis of the proteomics from the above four testing groups, we identified three distinct protein groups closely associated with LLPS, namely LLPS-aboriginal, LLPS-dependent, and LLPS-sensitive proteins. (Fig. 1c).

FUS-APEX2-EGFP fusion protein mediated proximity labeling in LLPS droplets

Firstly, we employed in vitro examinations to demonstrate that the FUS-APEX2-EGFP fusion tag did not interfere with the normal LLPS process of FUS. As shown in Fig. 2a, we found that the concentration of 10 mM NaCl could induce FUS-APEX2-EGFP protein for LLPS, which could be reversed by increasing the NaCl concentration (Supplementary Fig. 1a).

Furthermore, to investigate the controllability and efficiency of the condensation process of FUS-APEX2-EGFP protein into LLPS droplets, we explored the formation of LLPS droplets under sodium arsenite stimulation in living cells. We observed that under unstimulated conditions, only a few green fluorescence spontaneously aggregates, while the majority of fluorescence remained dispersed. This demonstrates that the spontaneous phase separation aggregation of FUS protein was random. Within 10 min of sodium arsenite stimulation, the droplets gradually condensed. The maximum radius of droplet formation occurred at 30 min. (Fig. 2b). We further performed fluorescence recovery after photobleaching (FRAP) to assess the mobility of FUS within the droplets. The result showed that the fluorescence signal in the droplets rapidly recovered to ~70% within 180 s after photobleaching (Supplementary Fig. 1b).

Next, to validate that APEX2 could perform biotin labeling of proteins within LLPS droplets, we used orange fluorescent dye conjugated with a streptavidin affinity tag to label FUS-APEX2-EGFP cells. Confocal images demonstrated that the green fluorescence of FUS-APEX2-EGFP in the diffused state co-localized with the orange fluorescence of the streptavidin-conjugated dye, indicating successful biotin labeling of surrounding proteins by the APEX2 (Fig. 2c). After 30 min of sodium arsenite stimulation, FUS protein condensed to form LLPS droplets, and the co-localization of the streptavidin-conjugated dye within the droplets confirmed the ability of the APEX2 to biotinylate proteins within the droplets. Next, we constructed transfected cells lacking FUS protein and transfected cells lacking APEX2 protein as control groups, namely CON-APEX2-EGFP and FUS-CON-EGFP. In CON-APEX2-EGFP cells, diffuse fluorescence of the streptavidin-conjugated dye was observed, indicating biotinylation of surrounding proteins by APEX2, but no formation of condensed droplets. In FUS-CON-EGFP cells, green fluorescence was observed, but no orange fluorescence of the streptavidin-conjugated dye was detected, indicating that the presence of APEX2 was required for biotinylation. Taken together, these results implied that the CLAPM strategy could rapidly, effectively, and controllably label proteins in LLPS droplets. In addition, we performed Western Blot experiments on cell lysates from cells transfected with the FUS-APEX2-EGFP protein and wild-type cells. We observed electrophoretic bands of the FUS-APEX2-EGFP protein for transfected cells, as well as two lighter sub-bands resulting from the cleavage of the FUS-APEX2-EGFP protein. No electrophoretic bands were observed for wild-type cells. (Fig. 2d).

We then used streptavidin-modified magnetic beads to enrich biotinylated proteins from the cell lysate after proximity labeling. Western blot analysis of the elution from the magnetic beads confirmed the capturing ability of the beads for intracellular biotin tags (Supplementary Fig. 1c). We employed isotopic quantitative mass spectrometry to

https://doi.org/10.1038/s41467-025-59457-z

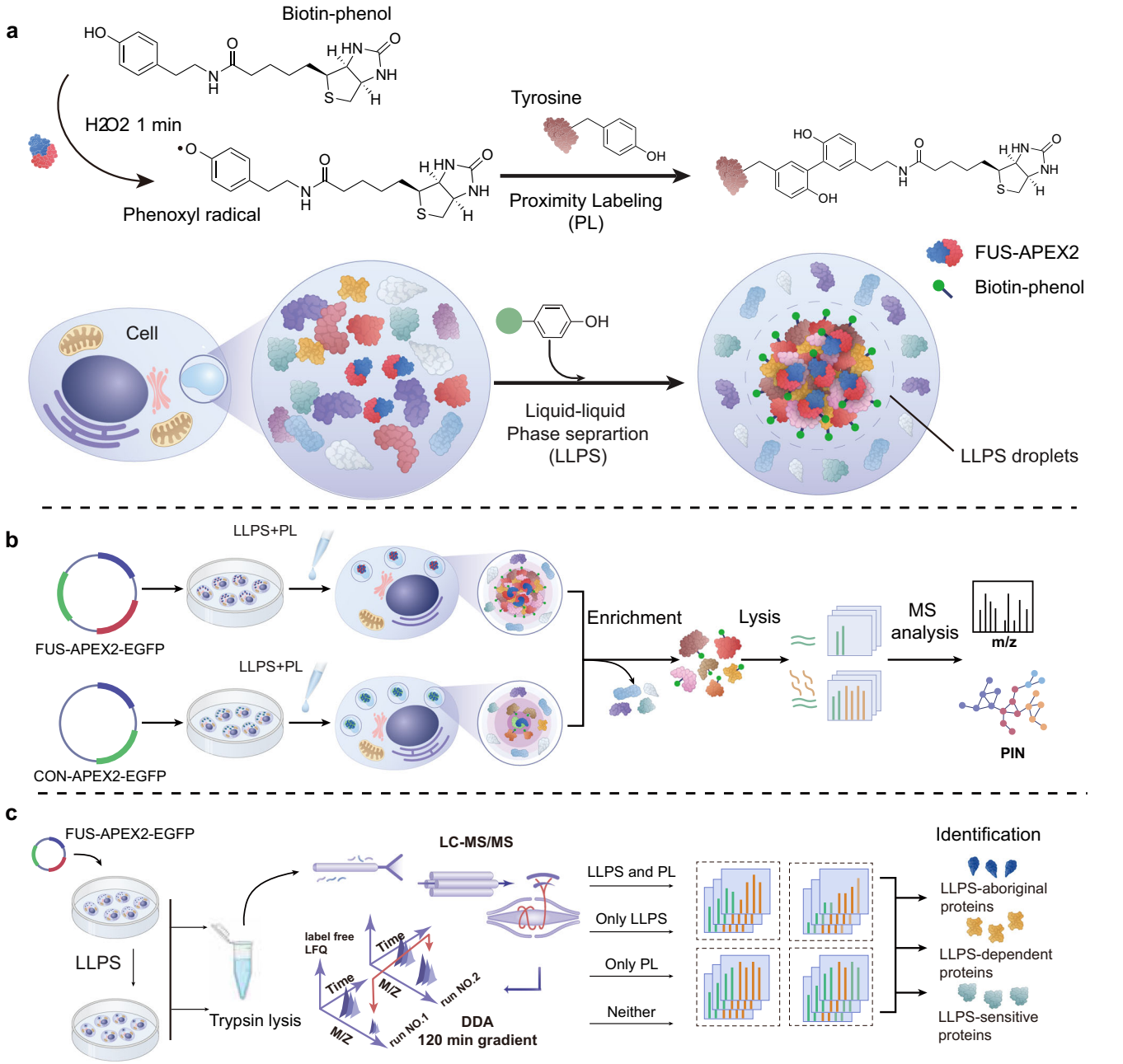

Fig. 1 | Schematic representation of the Composition of FUS Interactome Assembly by Proximity labeling assisted Mass spectrometry (CLAPM) strategy. **a** The CLAPM strategy for dynamic and transient analysis of proteomics within droplets that undergo Liquid-liquid phase separations (LLPS). LLPS is induced by adding sodium arsenite to stimulate the assembly of the FUS protein (blue) into condensed droplets. In H_2O_2, the ascorbate peroxidase enzyme APEX2 (red) converts biotin-phenol into a phenoxyl radical, which reacts with the adjacent tyrosine residues. Proximity labeling (PL) is achieved through in situ enzymatic synthesis of a biotinylated reaction intermediate, which subsequently diffuses and reacts with nearby proteins. The nanoscale action radius of the intermediate (indicated by dashed lines) encompasses both tightly bound proteins interacting with the bait and loosely interacting proteins within the same compartment, allowing PL to capture multi-layered protein-protein interactions in droplets. **b** Flow chart describing the steps for identifying candidate LLPS proteins by CLAPM. FUS-APEX2-EGFP cells represent the experimental group, and CON-APEX2-EGFP cells represent the control group. We simultaneously initiated LLPS and PL by adding substrates for PL and LLPS inducers. After cell lysis, biotinylated proteins were collected through affinity purification and characterized using mass spectrometry to analyze the protein-protein interaction networks (PIN) within the LLPS droplets. **c** The schematic diagram illustrates the quantitative analysis of biotinylated proteins using mass spectrometry (MS). We employed the Orbitrap Liquid Chromatography-Mass Spectrometer (LC-MS) to perform Data-Dependent Acquisition (DDA) analysis on the digested peptides. We conducted conditional controls by examining the presence of FUS protein, the addition of PL substrates, and the induction of LLPS by sodium arsenite stimulation. After statistical analysis of the MS data, we uncovered the proteome composition within the LLPS droplets was an orchestra of three categories, termed as LLPS-aborigines, LLPS-dependent, and LLPS-sensitive proteins.

determine the abundance of proteins. The heavy group represents proteins containing 15 N and 14C-labeled lysine, while the light group represents proteins with normal lysine. Protein identification and quantification of heavy to light (H/L) ratios were highly reproducible across replicate experiments (Supplementary Fig. 1d).

CLAPM specifically biotinylated FUS Interactome

Next, we investigated CLAPM for deciphering protein interactions in complex LLPS droplet environments. To exclude the diffuse labeling of FUS and the non-specific adsorption of endogenously biotinylated proteins or streptavidin beads, we conducted conditional controls by

https://doi.org/10.1038/s41467-025-59457-z

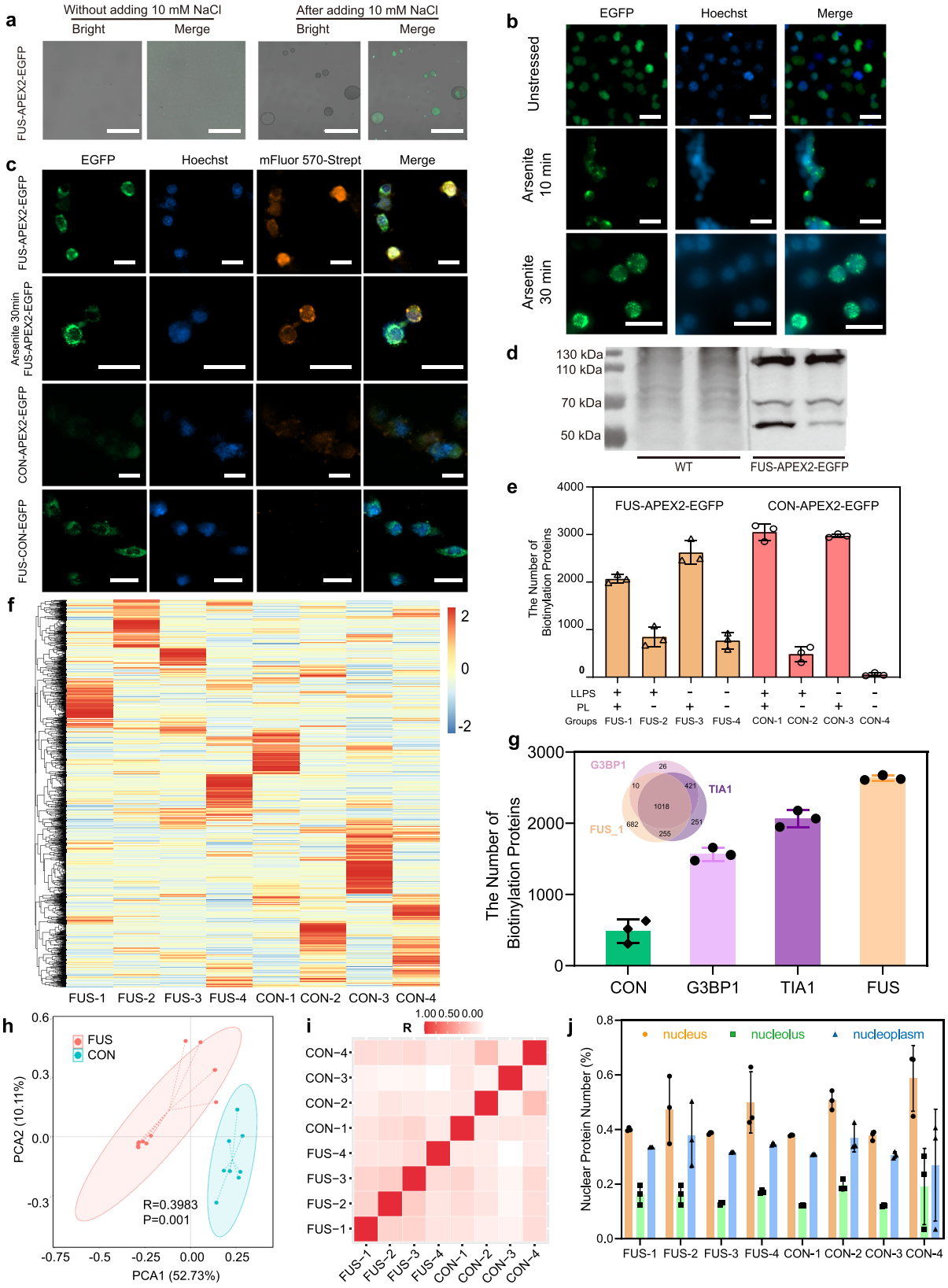

examining the presence of FUS protein, the addition of PL substrates, and the induction of LLPS with sodium arsenite stimulation. The FUS-1 group was stimulated with both sodium arsenite and PL substrate. The FUS-2 group was stimulated with only sodium arsenite. The FUS-3 group was treated with only the PL substrate. The FUS-4 group was treated with neither stimulus nor PL substrate. The cells expressing CON-APEX2-EGFP protein were named as CON group. The CON group followed the same numerical naming convention as the FUS group (Fig. 2e).

In the FUS-1 group (under the presence of FUS protein, addition of PL substrates, and induction of LLPS), we identified over 2000 proteins. In the FUS-3 group (without sodium arsenite stimulation) and

Fig. 2 | Identification of specific biotinylated proteome using the CLAPM method with FUS-APEX2-EGFP fusion protein. a The FUS-APEX2-EGFP fusion protein forms phase-separated droplets in vitro at a NaCl concentration of 10 mM. The scale bar is 20 μm. **b** The process of FUS protein condensation into LLPS droplets is induced by sodium arsenite stimulation in living cells. The FUS protein condensed into LLPS droplets after 30 min. The scale bar is 20 μm. **c** Fluorescent staining with streptavidin (Strept) confirms the biotinylation of proteins inside the droplets using CLAPM. The images demonstrate the colocalization of biotinylated proteins and the APEX2 enzyme. In the control group lacking APEX2, no biotinylation occurred, resulting in no detection of streptavidin fluorescence. The scale bar is 20 μm. **d** Western blot images confirm the successful expression of the FUS fusion protein in cells. **e** The number of biotinylated proteins identified in the FUS groups and the control groups. The cells expressing FUS-APEX2-EGFP protein are named as the FUS group. The cells expressing CON-APEX2-EGFP protein are named as the CON group ($n = 3$ biological replicates for each condition). **f** Heatmap showing the characteristic protein enrichment of the proximity-labeled proteome in the FUS groups and control groups. The heatmap is based on the abundance intensities of the proximity-labeled proteome normalized after unsupervised hierarchical clustering. **g** The number of biotinylated proteins identified in LLPS droplets in the FUS, G3BP1, TIA1, and the control groups. Venn diagrams show protein overlap in FUS, G3BP1, and TIA1 groups ($n = 3$ biological replicates for each condition). **h** Principal component analysis (PCA) showing the difference in protein enrichment between the FUS groups and CON groups. Statistical analysis used a two-tailed unpaired t test. **i** Correlation heatmap showing a significant difference in the proximity-labeled proteome between FUS groups and CON groups. **j** The proportion of nuclear proteins in each group identified by the CLAPM ($n = 3$ biological replicates for each condition). The above data in Fig. 2e, g, and j are presented as mean values +/− SD. The above Source data are provided as a Source Data file.

CON-1 group (without FUS protein), 2500 and 3000 proteins were identified, respectively. The reason for the increased number of identified proteins could be the improper condensation of LLPS droplets, resulting in a significant amount of dispersed biotin labeling. In the CON-4 group (without any conditions), only about 100 proteins were identified. The low number of proteins may originate from non-specific adsorption to the magnetic beads. We utilized an empirical Bayesian approach based on Linear Modeling of Microarray Data (LIMMA) to identify significantly enriched proteins in biotinylated samples. The LIMMA method uses observed data to estimate the global sample variance to adjust individual protein variances[40]. We employed an improved Benjamini-Hochberg false discovery rate (FDR) method to correct the obtained adjusted p-values and determine the adjusted q-values[41,42]. The FDR values of all peptides and proteins were less than 1%. The hierarchical clustering heatmap showed that each experimental group had a unique set of highly abundant proteins (Fig. 2f). Each experimental group was in triplicate, and the violin group with protein abundance in each group indicated robust intra-reproducibility (Supplementary Figs. 1e & 2e).

To investigate whether the CLAPM deploys the same biotinylated markers to respond to different models of LLPS, we performed proteomic characterization after capture of the biotinylated in HEK 293 T cells exposed to heat stress (42 °C), oxidative stress (sodium arsenite), osmotic stress (sorbitol), or ultraviolet (UV) stress[42,43]. Confocal images demonstrated that FUS-APEX-EGFP could form LLPS droplets under different stress conditions. Mass spectrometry identification indicated that the LLPS for all models led to an increase in biotinylated proteins. We detected approximately 5000 biotinylated proteins in four LLPS models, including 61% (4149/6785) of overlapping hits. (Supplementary Fig. 2a).

To further validate the effectiveness of CLAPM in LLPS mediated by different proteins, we also constructed G3BP-APEX2-EGFP and TIA1-APEX2-EGFP fusion proteins and performed interactome analysis in LLPS droplets in HEK 293t cell[44,45]. Confocal images demonstrated the formation of LLPS droplets was similar to FUS. We also observed the co-localization of orange streptavidin immunofluorescence and green EGFP fluorescence, demonstrated biotinylation of the G3BP1 and TIA1 interactome in LLPS droplets (Supplementary Fig. 2b,c). Each experimental group was in triplicate, and the scatterplot indicated robust intra reproducibility (Supplementary Fig. 2d). In the groups of G3BP1, TIA1, and FUS, we identified 1500, 2000 and 2300 proteins, respectively, far exceeding the number of biotinylated proteins in the control group (CON-APEX2-EGFP and no PL conditions) of around 300. Of nate, the interaction group of the three proteins shared 45% (1018/2263) of common hits (Fig. 2g). We retrieved protein-protein interaction data for 99 proteins whose G3BP1 and TIA1 interactome in LLPS intersects with known LLPS proteins (Supplementary Fig. 2e). The generated LLPS-PIN contains 99 nodes and 371 non-redundant edges. We analyzed ten frequently reported known LLPS proteins and found that they shoed abundance disparities in different LLPS droplets (Supplementary Fig. 2g). HSP proteins are more inclined to appear in FUS droplets. EIF3B is more inclined to appear in TIA1 droplets. DDX21 and DDX5 proteins have little inclination. The principal component analysis (PCA) demonstrated a clear separation between the protein profiles of the FUS groups and the CON groups (Fig. 2h). The correlation heatmap showed that the correlation R values between the FUS and CON groups were both less than 0.5 (Fig. 2i).

CLAPM revealed FUS Interactome in LLPS droplets under FUS disease mutations

We performed the cellular component analysis of proteins identified by CLAPM. Our results revealed that nearly 40% of the biotinylated proteins were nuclear proteins across the eight experimental groups (Fig. 2j). Previous studies have demonstrated that neurodegenerative diseases are closely associated with erroneous LLPS localization of FUS in the cytoplasm. Thus, to obtain the FUS interactome composition in LLPS droplets specific to the cytoplasm, we further utilized a cell model of FUS^{P525L} aggregation. FUS^{P525L} is an ALS-associated mutation that disrupts the nuclear localization of FUS and causes its aggregation specific in the cytoplasm (Fig. 3a). We generated $FUSP^{525L}$-APEX2-EGFP protein constructs in both HeLa and HEK 293 T cells. CLAPM identified over 2500 proteins in both the HeLa cells and the HEK 293 T cells. The number of identified proteins increased by 500 compared to the non-mutated cell model with FUS-APEX2-EGFP (Fig. 3b, c). We named the group expressing FUS^{P525L}-APEX2-EGFP protein as the EXP group, distinguishing from the group expressing wild-type FUS protein. Meanwhile, the CON group only expressed the APEX2-EGFP protein. The green fluorescent signal indicated the FUS^{P525L}-APEX2-EGFP protein was not expressed in the cell nucleus (Fig. 3d). The FUS^{P525L}-APEX2-EGFP protein was localized specifically in the cytoplasm and condensed to form LLPS droplets.

In HeLa cells, granules of the EXP groups tended to cluster together, while the granules of the CON groups were more scattered (Fig. 3e). The PCA plot suggests that the protein composition in the EXP groups is similar, and the CON groups contain a more diverse range of protein composition. The majority of proteins identified in the CON groups originated from non-specific biotin labeling of FUS^{P525L}-APEX2-EGFP protein within the cells. The correlation heatmap showed that the within-group correlation (R-value) for the four EXP groups is more than 0.75 (Fig. 3f). The inter-group correlation (R-value) among the four EXP groups is approximately 0.5. In contrast, the inter-group correlation (R-value) for the four CON groups is less than 0.5, and the correlation (R-value) between the CON groups and the EXP groups is less than 0.25. The violin plot illustrates the identified protein abundance distribution by CLAPM in HeLa cells lacking nuclear localization (Fig. 3g). We adopted CLAMP to identify a total of 5814 proteins in both the HeLa and HEK 293 T cell models. We identified 3693 proteins that HeLa and HEK 293 T cells commonly shared, with 760

https://doi.org/10.1038/s41467-025-59457-z

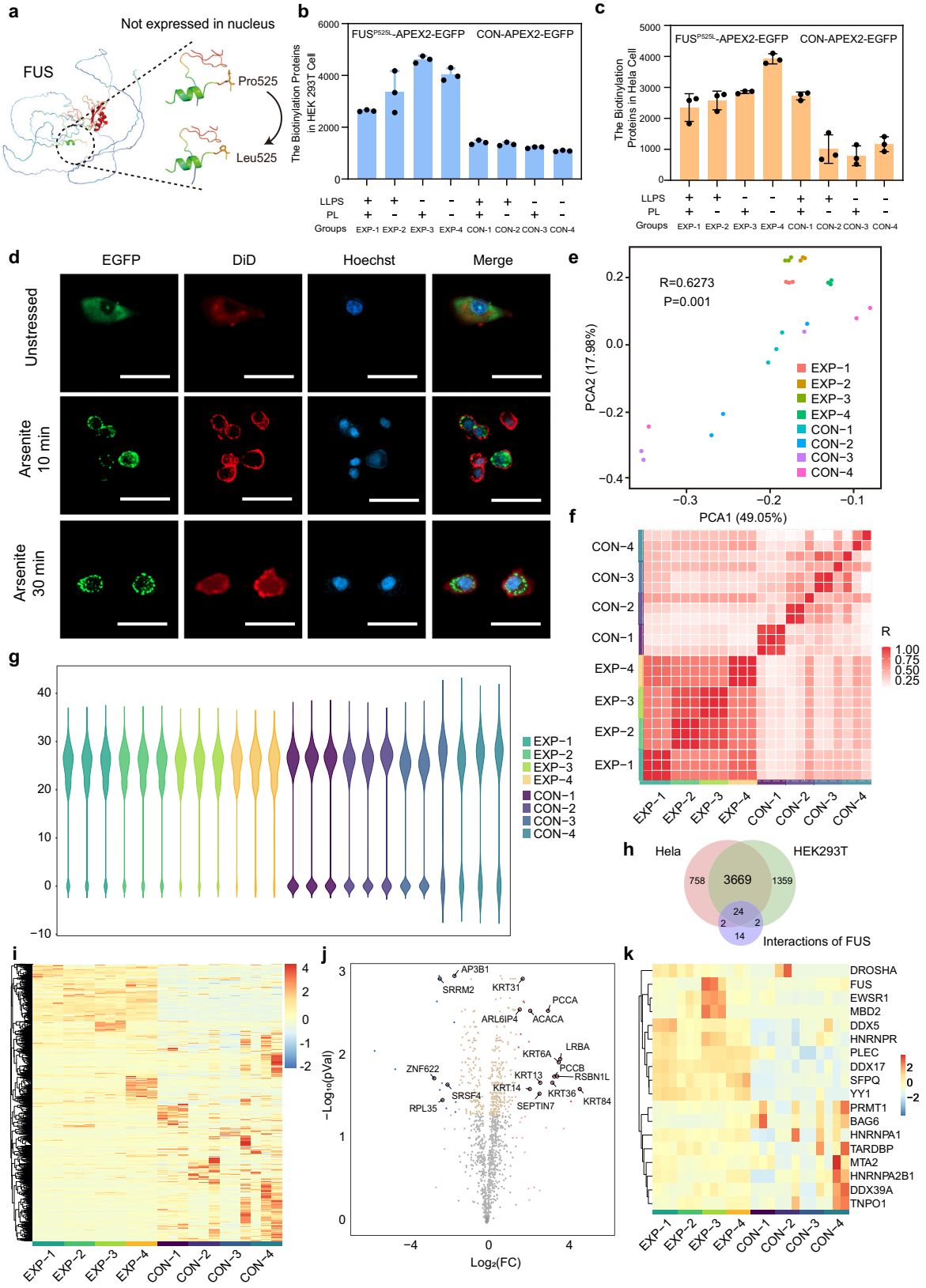

proteins unique to HeLa cells and 1361 proteins unique to HEK 293 T cells (Fig. 3h). The highly abundant proteins and the lowly abundant proteins exhibit a polarized trend. The hierarchical clustering heatmap showed the distribution of unique, highly abundant proteins in the EXP groups (Fig. 3i). The proteins that are specifically highly abundant in the EXP groups are considered candidates for the protein composition within LLPS droplets. The relevant data from HEK 293 T cell is also included in the supplementary information (Supplementary Fig. 3).

Among all the 42 known proteins to interact with FUS, CLAPM identified 28 proteins, accounting for 66.7% (28/42). The volcano plot displayed significantly enriched proteins within the EXP groups in

Fig. 3 | Identification of biotinylated proteins by CLAPM in disease mutation models. a Schematic of the FUS protein with a disease-associated mutation, where serine amino acid residue 525 is replaced by leucine. **b** The number of biotinylated proteins identified in LLPS droplets formed by the mutated FUS protein was assessed under eight experimental conditions in HEK 293 T cells ($n = 3$ biological replicates for each condition). **c** The number of biotinylated proteins identified in LLPS droplets formed by the mutated FUS protein was assessed under eight experimental conditions in HeLa cells ($n = 3$ biological replicates for each condition). **d** The confocal images show the formation of LLPS droplets by FUS^{P525L}-APEX2-EGFP fusion protein. Green and blue fluorescence do not co-localize, demonstrating that FUS^{P525L}-APEX2-EGFP was not expressed in the cell nucleus. The scale bar is 20 μm. **e** Principal component analysis (PCA) plot showing the difference in proteome between EXP groups and CON groups in HeLa cells. Statistical analysis used a two-tailed unpaired *t* test. **f** Heatmap of correlation showing the differences in proteome enrichment between EXP groups and CON groups in HeLa cells. **g** The violin plot shows the distribution and probability density of protein types and abundances within EXP groups and CON groups. The vertical axis represents the logarithm (base 2) of the protein abundance after normalization. **h** Venn diagram showing the overlap between known interaction proteins of FUS and CLAPM hits identified in HeLa and HEK 293 T cells. **i** Heatmap showing the detailed proteome enrichment differences between experimental and control groups. **j** Volcano plot showing statistically significant enrichment of proteins in EXP-1 and EXP-2. The horizontal axis represents the fold change, and the vertical axis represents the significance of the difference. Statistical analysis used a two-tailed unpaired *t* test. **k** Heatmap showing the abundance of known LLPS proteins and FUS-interacting proteins enriched in the proximity-labeled proteome by CLAPM. The above data in Fig. 3b, c are presented as mean values +/− SD. The above Source data are provided as a Source Data file.

HeLa cells (Fig. 3j). Among them, several well-characterized proteins (such as RNF213 and SRSF4) are known critical proteins involved in LLPS[46–49]. We also discovered proteins that interact with known LLPS proteins (such as HNRNPR) or family proteins closely related to LLPS[50]. For example, DDX1, a known member of the DEAD-box helicase family, was reported to be localized within LLPS droplets and was crucial to the formation of RNA transport complexes[51]. CLAPM revealed other members (DDX5 and DDX17) of this family located within LLPS droplets. Figure 3k illustrates the significant enrichment of known LLPS proteins in the EXP group, demonstrating that CLAPM could faithfully identify FUS interactome composition in LLPS droplets in cells with disease-associated mutations. Notably, not all protein enrichment results from the EXP groups could be considered as candidates for FUS interactome composition in LLPS droplets. For example, some keratins (KRT) were erroneously identified as enriched proteins. The reason for this could be attributed to the widespread distribution of KRT proteins and the erroneous results caused by droplet enrichment near the cytoskeleton.

Establishment of dynamic FUS Interactome in LLPS droplets by CLAPM

Proximity effects dynamically occur for the FUS interactome during translation. Endogenous biotinylated proteins also appear in the process of protein enrichment after proximity labeling. Magnetic nanoparticles could exhibit non-specific adsorption. Therefore, we defined false-positive proteins as endogenous biotinylated proteins, randomly located droplets, and biotinylated proteins produced by the FUS translation process, as well as non-specific bead adsorption proteins. We established a FUS-mediated dynamic proteomes model in the LLPS coalescence process. The biotinylated proteins could be divided into three types of dynamic proteomes: 1) LLPS-aboriginal proteins, which are unrelated to LLPS and have interact with FUS protein; 2) LLPS-dependent proteins, which are only related to FUS when LLPS occurs; 3) LLPS-sensitive proteins, whose association with FUS is weakened or lost due to LLPS (Fig. 4a). We systematically identified the three types of proteins and removed false-positive proteins using a series of quantitative proteomics logistics. We designed five experimental groups to distinguish the above dynamic proteomes (Fig. 4b). First, to identify stress-dependent FUS interaction factors, we compared FUS^{P525L}-APEX2-EGFP cells with and without the occurrence of LLPS under PL conditions (Group 1). Next, we compared FUS^{P525L}-APEX2-EGFP cells with and without PL under LLPS conditions (Group 2). Third, we compared FUS^{P525L}-APEX2-EGFP cells with and without PL under LLPS conditions to distinguish diffuse biotin labeling (Group 3). Then, we compared the lysates of FUS^{P525L}-APEX2-EGFP and CON-APEX2-EGFP cells under LLPS conditions to distinguish endogenous biotin labeling (Group 4). Finally, we compared non-LLPS FUS^{P525L}-APEX2-EGFP and CON-APEX2-EGFP cells (Group 5) to determine the dependency and sensitivity of FUS interaction factors. Based on the following analysis steps, we identified the aforementioned three types of dynamic proteomes. First, we compared the enrichment of known LLPS proteins in Fig. 3j to the background distribution of proteins from the quantitative proteomic data in the HeLa cells (Fig. 4c). We used known LLPS proteins to determine a cutoff for the ratio of the experimental groups. We sorted proteins in the above Groups based on the known LLPS proteins' $\log_2$ ratio and calculated the frequency distribution of known LLPS proteins in the sorted list. Most known LLPS proteins in Fig. 3J were significantly enriched in Groups 1, 2, 4, and 5, with detected ratios approaching or exceeding 2-fold. We thus chose 2-fold as the conservative critical value for enrichment and removed proteins below 2-fold for further analysis.

The volcano plot displays proteins with significant differences. The comparison of enriched proteins in Group 1 reveals proteins that are biotinylated due to LLPS-mediated proximity labeling (Fig. 4d). This includes proteins from the DDX family, Heat Shock Proteins (HSP) family, and KRT family. The comparison in Group 2 can identify biotinylated proteins related to proximity labeling (Fig. 4e). In this group, we not only found proteins from the DDX and KRT families but also STRAP, EIF3E, and SF3A1 that were known to interact with FUS or be associated with RNA. The comparison in Group 3 could identify proteins that interact with FUS before LLPS occurs (Fig. 4f). This includes members of the HSP family (HSPE1 and HSPA5) and PARK7. Comparisons in Group 4 and Group 5 showed false positives and non-specific bindings due to non-FUS-mediated interactions. In Group 4, we also found members of the DDX family and HSP family (Fig. 4g). Proteins identified in Group 5 mainly originated from non-specific adsorption to the magnetic beads, with small significance differences (Fig. 4h). We observed that known LLPS proteins appeared to exhibit an enrichment trend in the absence of stress (Group 5). For the final list of LLPS candidate proteins, we selected proteins that were enriched in all three replicate experimental groups above 2-fold. We defined a set of 83 proteins as LLPS-dependent and another set of 46 proteins as LLPS-aboriginal from Groups 1, 2, 4, and 5 (Fig. 4i). A detailed list of these proteins can be found in the supplementary materials (Supplementary Data 1). In addition, we defined a set of 90 proteins as LLPS-sensitive (Supplementary Fig. 4a) at the intersections of Groups 1, 2, 3, and 5. The relevant data from HEK 293 T cells is included in the supplementary information (Supplementary Figs. 4, 5b and Supplementary Data 2).

The identified LLPS proteins, such as DDX21, DDX27, HSP90AB1, and SERBP1, have been previously recognized as crucial proteins interacting with FUS[37,52,53]. For example, DEAD-box helicase (DDX21 and DDX27) is known to localize to LLPS and has been shown to form RNA transport complexes. We found that over half (64.3% [83/129]) of the proximity-labeled proteins were LLPS-dependent proteins. Notably, 35.7% (46/129) of proximity-labeled proteins were LLPS-aboriginal proteins with FUS, even in the absence of LLPS. LLPS-aboriginal proteins also include HSP90AB1, HSPA5, SERBP1, and EEF1D. SERBP1 has recently been found to harbor ALS-associated mutations that lead to abnormal protein aggregation.

https://doi.org/10.1038/s41467-025-59457-z

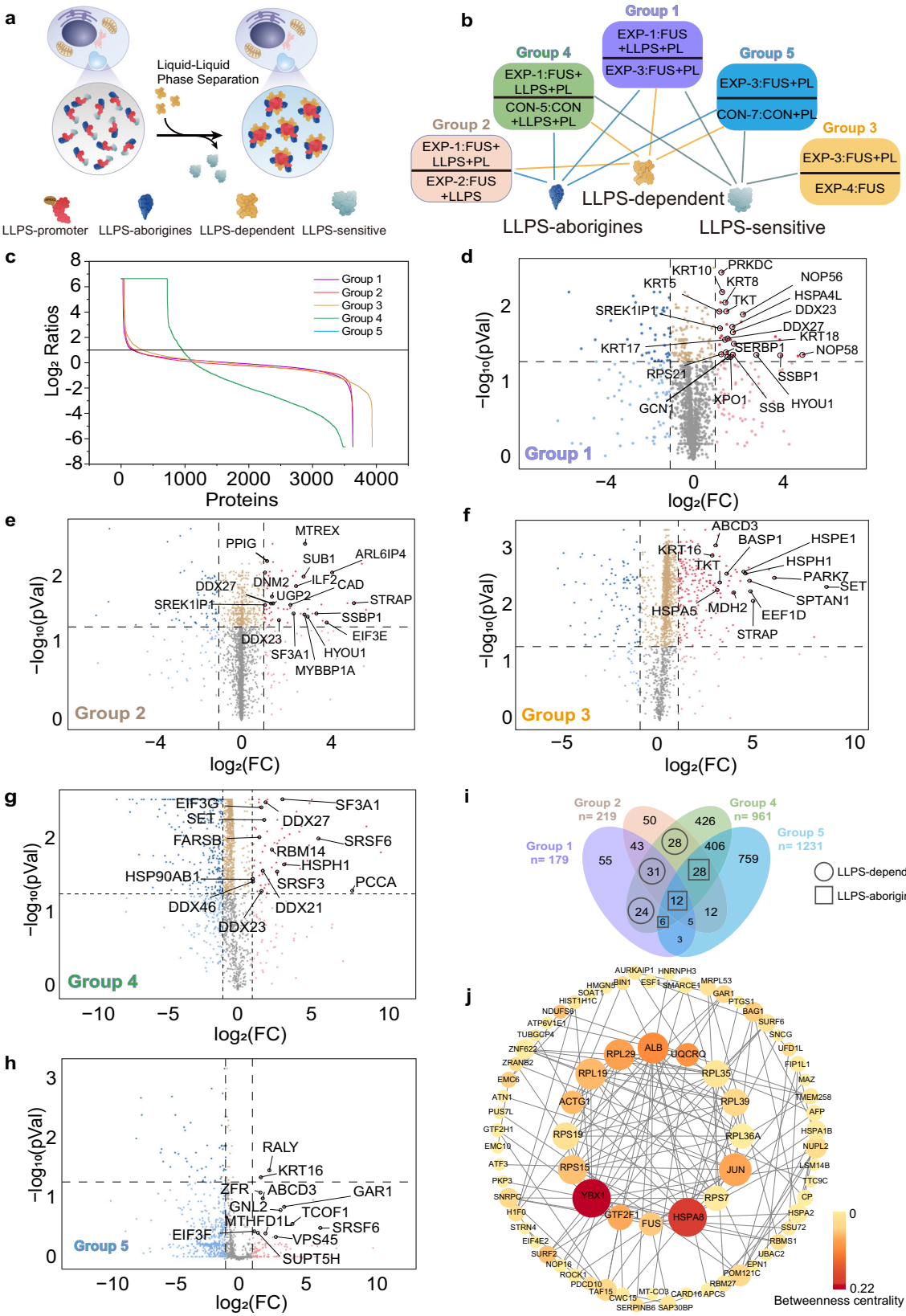

Construction of Protein interactions between LLPS-dependent proteins and LLPS-aboriginal proteins

We retrieved protein-protein interaction (PPI) data for the LLPS-dependent proteins and LLPS-aboriginal proteins in HeLa cells. The generated LLPS-PIN contained 183 nodes and 340 non-redundant edges (Fig. 4j). Combined with LLPS-aboriginal proteins interacting with FUS before LLPS occurs, pre-existing protein interaction steady-state networks may facilitate the rapid aggregation of LLPS visible under the microscope when cells were exposed to environmental stress. Gene Ontology (GO) enrichment analysis showed that transcription regulation, RNA processing, heat shock response regulation, and splicing complexes were among the main signaling pathways,

Fig. 4 | Establishment of dynamic proteomes and protein interactions in LLPS droplets. a The schematic diagram shows the dynamic proteome composition shift during FUS condensation into droplets. **b** The experimental design for decoding proteome composition heterogeneity within droplets. **c** The logarithmic plot of protein abundance ratios in the five groups is displayed from the HeLa cell model. The maximum value of the ratio is normalized to 100, and the minimum value is normalized to 0.01. **d** The volcano plot demonstrates the statistically significant enrichment of proteins in Group 1. Group 1 represents the impact of liquid-liquid phase separation on the differential labeling of biotinylated proteins. **e** The volcano plot demonstrates the statistically significant enrichment of proteins in Group 2. Group 2 is the comparison of differences in LLPS that occurs within the experimental group, aiming to screen for endogenous and non-specific biotin labeling. **f** The volcano plot demonstrates the statistically significant enrichment of proteins in Group 3. Group 3 represents the comparison between experimental groups where no LLPS occurred. The purpose of this comparison is to screen for interacting proteins that exclude liquid-liquid phase separation and to exclude proteins with diffuse biotin labeling. **g** The volcano plot demonstrates the statistically significant enrichment of proteins in Group 4. Group 4 compared the differences in biotinylated protein labeling mediated by FUS, aiming to screen for diffusely biotinylated proteins. **h** The volcano plot demonstrates the statistically significant enrichment of proteins in Group 5. Group 5 aims to eliminate non-specific and endogenous biotin labeling. The horizontal axis represents the fold change, and the vertical axis represents the significance of the difference in all volcano plots. Statistical analysis used a two-tailed unpaired *t* test. **i** Venn diagram showing the overlap between Groups 1, 2, 4, and 5. **j** The protein-protein interaction network identified as LLPS-dependent protein and LLPS-aboriginal protein in HeLa cells is shown. The network was visualized in Cytoscape. The discrete color scale is used to represent the betweenness value, and the area of the circle represents the degree value. Source data are provided as a Source Data file.

where LLPS proteins were enriched (Supplementary Fig. 5a). Among the GO enrichment analysis, 70% of LLPS-dependent proteins and LLPS-aboriginal proteins in LLPS droplets mainly mediate RNA-related physiological processes, which is similar to the physiological function of FUS.

Dynamic FUS Interactome compositions in LLPS droplets from living neuronal cells

SH-SY5Y cells are a typical cellular model for neurodegenerative diseases. We induced SH-SY5Y differentiation to obtain sustainable cells with mature human neuronal morphology and biochemical characteristics of neurons. Subsequently, we used a lentiviral vector to introduce endogenous expression of the FUS^{P525L}-APEX2-EGFP protein in SH-SY5Y cells. FUS^{P525L}-APEX2-EGFP robustly localized to LLPS droplets upon $NaAsO_2$ treatment, and streptavidin staining overlapped well with the EGFP signal (Fig. 5a). These characteristics were consistent with those observed in HeLa cells. We then utilized CLAPM to analyze the proteome composition within LLPS droplets in SH-SY5Y cells expressing FUS^{P525L}-APEX2-EGFP. The experimental setups for Groups EXP 1-4 were similar to those in HeLa cells. Additionally, we established CON-APEX2-EGFP cells as a control. The CON-1 group was stimulated with sodium arsenite and treated with PL substrate. The CON-2 group was stimulated with sodium arsenite only.

We detected 3880 proteins in Group EXP-1, covering 77% of known LLPS proteins. The correlation heatmaps show that the within-group correlation (R-value) was greater than 0.8 for all four EXP groups (Fig. 5b). The between-group correlation (R-value) among the four EXP groups was approximately 0.6. In contrast, the between-group correlation (R-value) for the CON group was greater than 0.6, but the correlation between the CON group and the EXP group was less than 0.2. The violin plots illustrate the protein abundance distribution identified by CLAPM in the neural cells (Fig. 5c). In the EXP groups, there was a clear polarization between high and low abundance proteins, similar to what was observed in HeLa cells. However, in the CON groups, there were mainly low-abundance proteins, and almost no high-abundance proteins were detected. The hierarchical clustering heatmap reveals the unique and highly enriched distribution of proteins in the EXP-1 group, and high-abundance proteins exhibited significantly reduced abundance in the CON group (Fig. 5d). The highly enriched and specific proteins in the EXP groups were considered candidates for the protein composition within LLPS droplets. A detailed list of these proteins could be found in the supplementary information (Supplementary Data 3).

We repeated a similar analysis pipeline as in Fig. 4b to analyze the protein composition labeled by CLAPM in neural cells. The volcano plot shows proteins with significant differences in Groups 1, 2, and 3 (Fig. 5e). GO enrichment analysis of neural cells indicated that the cellular localization of the LLPS protein group was broad and exhibited high enrichment in ATP and metal ion binding. Compared with other cell models, neural cells exhibited biological processes of endocytosis, autophagy, and protein transport (Fig. 5f). We identified 596 LLPS-aboriginal proteins, 226 LLPS-dependent proteins, and 58 LLPS-sensitive proteins (Fig. 5g and Supplementary Fig. 7a, b). The protein composition of LLPS in neuronal cells not only included known RNA-binding proteins (RBPs) and several proteins associated with neurodegeneration (TDP43, NUMB1, and ZNF638), but also factors involved in autophagy and related vesicular transport, which modulated the clearance of aggregates, the second pillar of protein homeostasis. The LLPS-dependent protein group was able to form dense PINs with 224 nodes and 301 non-redundant edges (Fig. 5h).

Autophagy factors and RNA-binding proteins are highly correlated with the protein composition of LLPS droplets. This suggests that strict monitoring of FUS interactome through interactions with Heat Shock Proteins (HSPs) families may contribute to the crucial role of autophagy in heat shock clearance. It is noteworthy that we found a large number of proteins that localized to LLPS in neuronal cells, but did not observe so in at least one other examined cell model. Although proteins localized to LLPS may not be unique to LLPS in neuronal cells, we refer to them here as neuronal-specific FUS interactome due to their neuronal preference, as evidenced by their higher expression levels or cell-type-specific LLPS targeting. This systematic investigation of cell-type-specific LLPS further expands the list of LLPS proteins and suggests that neuronal cells exhibit greater diversity in LLPS composition than non-neuronal cells. Our observations indicate that previous studies using common immortalized cell lines may have missed potentially important neuronal LLPS proteins.

Validation of previously unreported LLPS proteins with neurodegenerative disease mouse model and public databases

Among the 226 LLPS-dependent proteins identified from our CLAPM dataset, 202 candidate LLPS proteins were previously unreported. To validate the potential relevance of these candidate proteins to neurodegenerative diseases caused by FUS pathological aggregation, we employed RT-qPCR to verify the expression of 16 LLPS-dependent proteins in brain tissues from two neurodegenerative disease mouse model versus wild-type mice (Fig. 6a). The APP/PS1 and SOD1 mouse models were selected due to their well-documented relevance in neurodegenerative diseases, as these models exhibit a high degree of genetic and physiological similarity to humans[54–57]. Furthermore, the well-characterized disease phenotypes associated with FUS protein in these models enabled us to efficiently achieve our research objectives. To minimize variability induced by hormonal fluctuations in female mice, male mice were utilized, ensuring consistent and reproducible results[58,59]. This approach allowed us to establish a controlled baseline for investigating protein expression levels in disease-associated brain tissues. TDP-43, a classical neurodegenerative disease-associated protein, was also included in the validation experiment. GAPDH proteins were used as internal reference proteins. Figure 6b is a schematic

https://doi.org/10.1038/s41467-025-59457-z

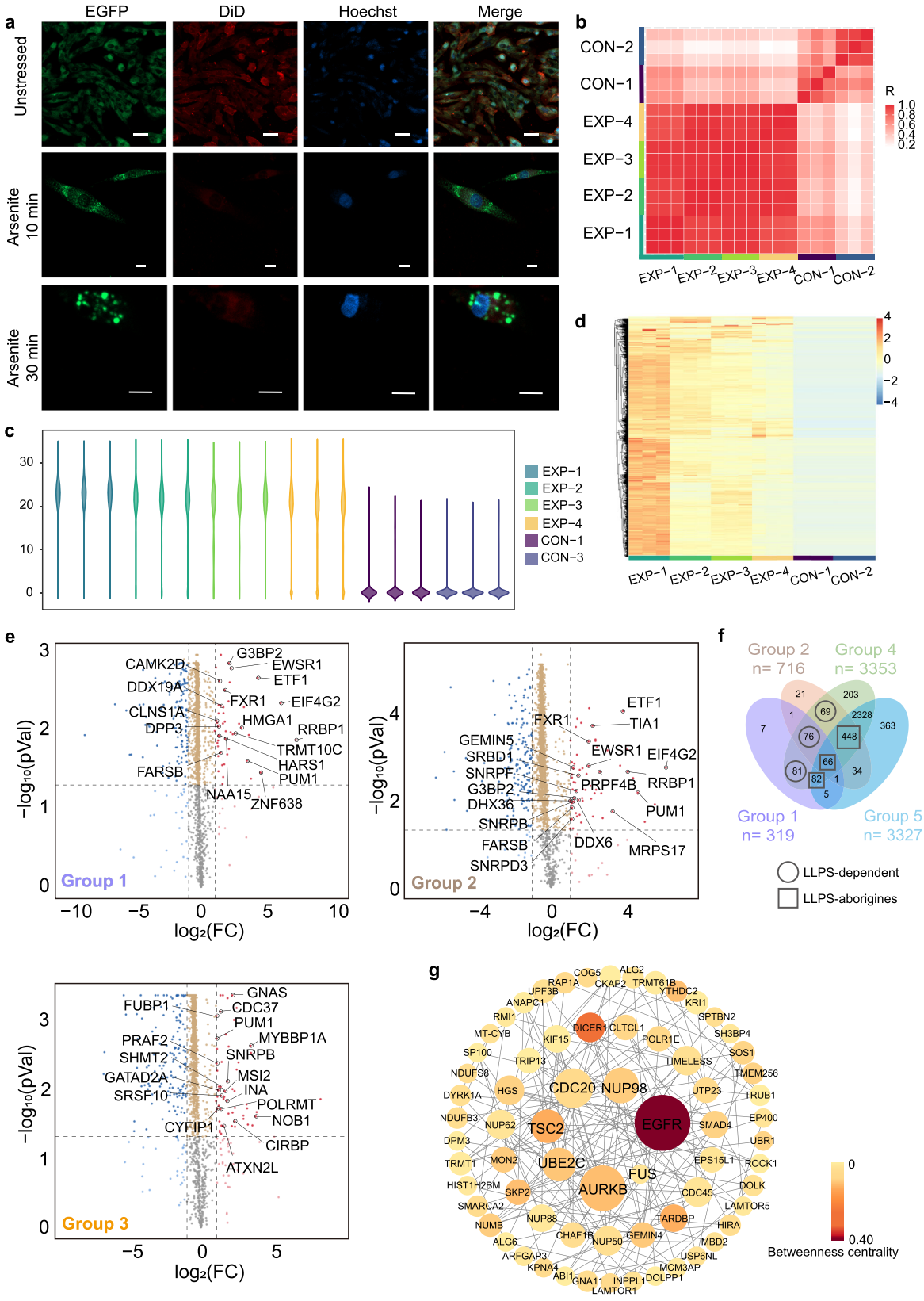

diagram of the brain partitions of the mouse, and we sampled the brain tissues of the SOD1 mouse and APP/PS1 mouse according to the locations shown for RT-qPCR experiments. 16 LLPS-dependent proteins (15 candidate LLPS proteins from our CLAPM dataset plus TDP-43) were found to be highly expressed in different brain regions compared with WT mice (Fig. 6c, d). The SOD1 mice exhibited 8 to 16-fold increased mRNA expression compared with wild-type mice in medulla, pituitary, striatum, hindbrain, and cerebellum. Compared with wild-type mice, the APP/PS1 mice showed almost 4 to 16-fold differential mRNA expression in the medulla oblongata, midbrain, and cerebellum. The differentially expressed in APP/PS1 mice were mainly concentrated in some brain regions (CB, MO, STR, MB) and specific

Fig. 5 | Dynamic proteome composition in LLPS droplets from living neuronal cells using CLAPM. a The confocal images show the formation of LLPS droplets by FUS^{P525L}-APEX2-EGFP fusion protein in non-stimulated neuronal cells and neuronal cells treated with arsenite. The scale bar is 20 μm. Green and blue do not co-localize, demonstrating that FUS^{P525L}-APEX2-EGFP is not expressed in the cell nucleus. **b** Heatmap of correlation showing the differences in proteome enrichment between experimental and control groups. **c** The violin plot shows the distribution and probability density of protein types and abundances in neuronal cells. The vertical axis represents the logarithm (base 2) of the protein abundance after normalization. The identified proteins in the control group were all low-abundance proteins since the biotin markers in the control group mainly came from non-specific adsorption and endogenous biotin, with almost no biotin markers coming from PL. **d** Heatmap showing the detailed proteome enrichment differences in neuronal cells. Heatmap is based on the abundance intensities of the proximity-labeled proteome normalized after unsupervised hierarchical clustering. **e** The volcano plot demonstrates statistically significant enrichment of proteins in Groups 1, 2, and 4. The horizontal axis represents the fold change, and the vertical axis represents the significance of the difference. Statistical analysis used a two-tailed unpaired *t* test. **f.** Venn diagram showing the overlap between Groups 1,2,4, and 5 in neuronal cells. **g** The protein-protein interaction network identified as LLPS-dependent protein and LLPS-aboriginal protein in neuronal cells is shown. The network was visualized in Cytoscape. The discrete color scale is used to represent the betweenness value, and the area of the circle represents the degree value. Source data are provided as a Source Data file.

proteins (like NUB1, SF3B5, CDC20, FOXP1, LSM1), while SOD1 mice showed increased mRNA expression in all brain regions. We observed a significantly higher proportion of Intrinsically Disordered Regions (IDR) and Low Complexity (LC) domains amino acid residues in both LLPS-dependent and LLPS-aboriginal proteins compared to background proteins (Fig. 6e, f). The average proportion of IDRs in LLPS proteins identified from HeLa, HEK 293 T, and SY-SH5Y cells was twice that of background proteins. The average proportion of LC domains in LLPS proteins identified from HeLa and HEK 293 T cells was also twice that of background proteins. The maximum proportion of LC domains in LLPS proteins identified from the SH-SY5Y cell model was twice that of background proteins. This is consistent with the recently proposed LLPS forming mechanism that IDR and LC domains were among the main intrinsic driving forces for LLPS[33].

We then integrated our CLPAM dataset with five previously published datasets related to protein aggregation in LLPS (Fig. 6g). Although the five public datasets did not completely overlap, their cross-comparison facilitate contextualize each individual study within a broader framework. Among the 226 LLPS-dependent proteins identified by CLAPM, 58 were found exclusively in CLAPM, and 15% of them were also found in at least half of the other datasets. Notably, many of these proteins exhibited a higher proportion of LC and IDR compared to the background proteome. EIF4B, SPTBN2, and DMX1 were known to be associated with neurodegeneration and were widely represented, along with several previously unknown LLPS proteins (for instance, CDC45, LSM1, FOXP1 and CHD5), warranting further investigation[60–67].

Discussion

We have developed CLAPM that permits spatiotemporally resolved identification of FUS interactome within LLPS droplets in living cells. CLAPM adopts proximity labeling, which has been used to identify molecular interaction types and analyze protein topology and surface moieties. Compared to traditional fluorescence labeling and in vitro simulation methods, CLAPM overcomes the insufficient number of fluorescent labels and false positives of conventional approaches. Moreover, CLAPM exhibits advantages for identifying low-abundance protein interactions and acquiring weak/transient protein interactions. When combined with mass spectrometry, PL technology can provide a dynamic FUS interactome at the spatiotemporal level, offering an enabling technique for gaining a deeper understanding of the molecular basis underlying composition within LLPS droplets.

Previous studies have identified the protein interactions in stress granules using proximity labeling techniques. Our study attempts to investigate the protein interaction in LLPS droplets in living cells. We have developed a FUS cellular model lacking nuclear localization, which is more analog to neurodegenerative disease phenotypes. We identified 129, 182, and 822 protein compositions in the LLPS droplets of Hela, HEK 293 T, and SH-SY5Y cells, respectively. Our results indicated that proteins may be recruited into LLPS droplets in a cell-type or LLPS-type specific manner. Neuronal cells appeared to harbor a more diverse set of LLPS components, many of which were reported to involve in the Protein Quality Control (PQC) pathway, such as chaperone-assisted protein folding, autophagic clearance of aggregates, and RNA-binding proteins. Defects in PQC have been associated with the development of neurodegenerative changes, and our observations may further elucidate why neuronal cells are particularly reliant on the precise regulation of protein homeostasis. We identified interactors of FUS that have not been previously reported to associate with LLPS. Among them, the CDC20-APC/C complex positively regulates the clustering of synaptic vesicles at the active zone to the presynaptic membrane in postmitotic neurons. DMXL2 acts as a scaffold protein on synaptic vesicles and potentially plays a critical role in neuronal and endocrine homeostasis. Insights into the pathogenesis of neurodegenerative diseases may be gained from CDC20 and DMXL2. FDXPl functions as a transcriptional repressor, while SF3B5 is an essential component of the splicing body complex. EIF4B is crucial for mRNA binding to the ribosome. In addition, RNA-binding proteins entering LLPS droplets may contribute to pathological cellular processes. Furthermore, our study was extended to encompass experimental mouse models. SOD1 is a model for amyotrophic lateral sclerosis (ALS), while APP/PS1 represents a disease model for Alzheimer's disease. The expression levels of the identified proteins were validated in different brain regions of the two disease model mice. The expression levels of the identified proteins were found to be significantly elevated in both the disease mouse model and the cellular model, with highly consistent results. This finding may provide insights into the study of neurodegenerative diseases.

In addition to acquiring a previously unknown dataset resource of LLPS candidate proteins, our study also connects known LLPS proteins with previously unrecognized LLPS proteins to human diseases and offers insights into the biology of LLPS with neurodegeneration. The presence of LLPS-aboriginal and LLPS-sensitive proteins clarifies the highly evolved and dense PPI network, which integrates many steps of gene expression regulation. Thus, although LLPS appears to be transient, its occurrence represents a tightly controlled balance of moderate and brief transitions in protein-protein interactions. Allocating high concentrations of proteins to interconnected protein complexes allows for efficient processing, but at the same time, it increases the risk of uncontrolled protein aggregation. Therefore, if transient protein aggregation within LLPS droplets is not properly resolved, it is likely to become a trigger for diseases, which also explains the presence of locally high concentrations of proteins in diseased tissues. Our findings demonstrate a close association between LLPS proteins and the heat shock protein signaling pathway, which could be one of the mechanisms for degrading LLPS droplets within organisms. Finally, CLAPM can be further optimized in terms of enzyme catalytic efficiency and substrate selection. A faster enzymatic process would better capture transient and weak protein-protein interactions. Improvements in non-toxic and better membrane-permeable PL substrates are also desirable. Moreover, the CLAPM can be used to further dissect the molecular architecture of LLPS droplets and distinguish closely related subtypes of LLPS granules, such as P-bodies and stress granules, as well as the characteristics of cell type-specific granules,

https://doi.org/10.1038/s41467-025-59457-z

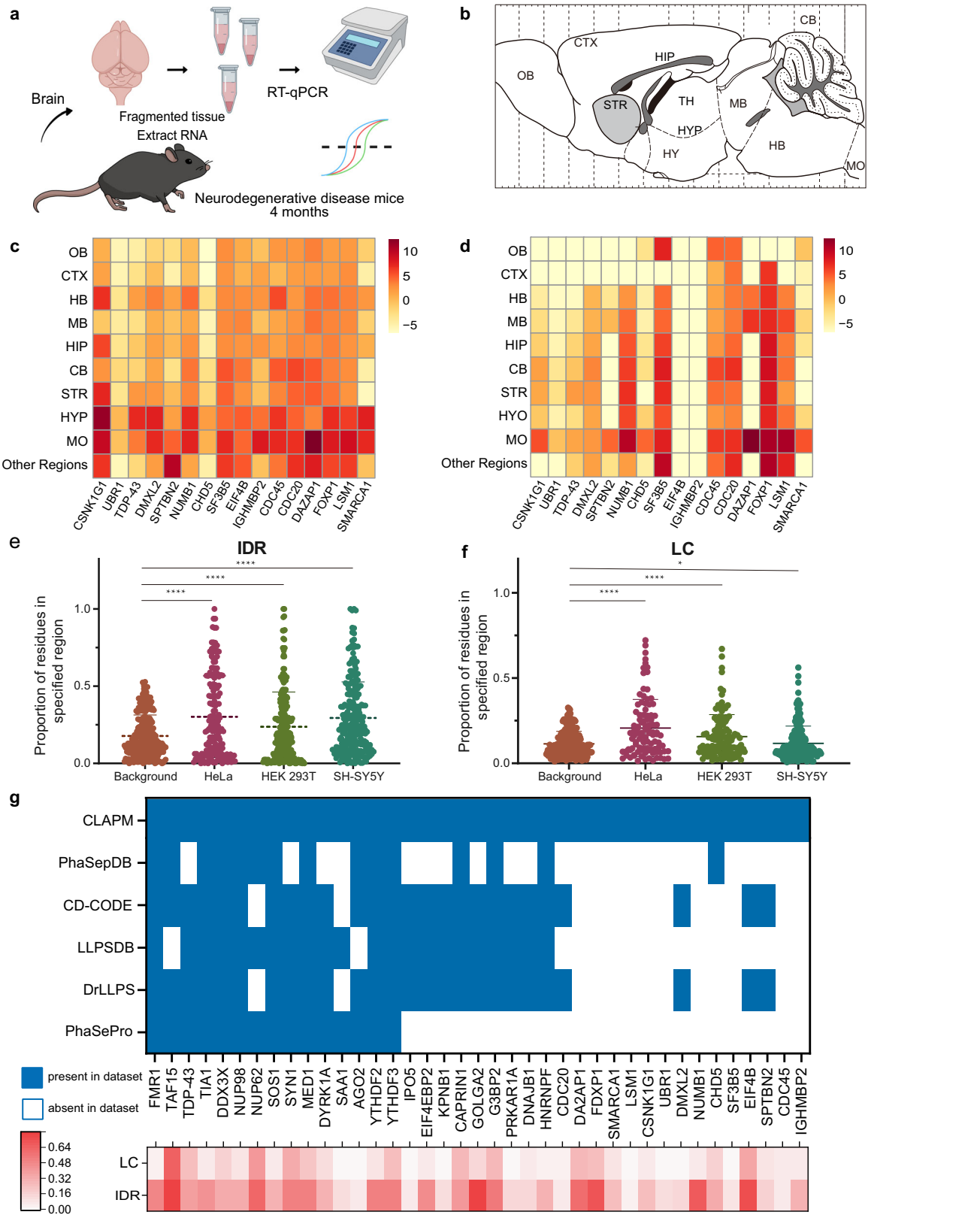

such as spermatid granules during spermatogenesis and ribosome biogenesis granules.

Methods

Ethical Statement

All experimental procedures were approved by the Institutional Biomedical Research Ethics Committee at the Institutional Animal Care and Use Committee (IACUC) of Shanghai Jiao Tong University, Shanghai, China (NO.202201309).

Animals

The APP/PS1 mouse is a gift from the Zhong Lab. of Shanghai Zhongshan Hospital. The SOD1 mouse was purchased from Shanghai Model Organisms Company. To avoid sex differences, all male mice were

Fig. 6 | Validation of previously unreported LLPS proteins with neurodegenerative disease mouse model and public LLPS databases. a Illustration of RNA extraction and RT-qPCR analysis from mouse brain tissue (Created with MedPeer [medpeer.cn]). The mouse model employed in this study comprises male mice aged 4 months, assigned to the experimental group, and an additional four wild-type mice as the control group. Mouse brain tissue samples were collected, and the total RNA was extracted. **b** Ten brain regions sampled from the mouse brain. OB, olfactory bulb; CTX, cortex; HB, hindbrain; MB, midbrain; HIP, hippocampus; CB, cerebellum; STR, striatum; HYO, hypophysis; MO, medulla oblongata; Other regions, including the thalamus, hypothalamus, superior colliculus, anterior commissure. **c** mRNA expression levels of the 16 target proteins in 10 brain regions of SOD1 mice. **d** mRNA expression levels of the 16 target proteins in 10 brain regions of APP/PS1 mice. RT-qPCR data were normalized by the expression of the reference protein GAPDH. The data in the heat map are log2 processed $2^{-\Delta\Delta Ct}$. **e**, **f**. The scatter plot illustrates (**e**) the ratio of Intrinsically Disordered Regions (IDR) to the total sequence length in LLPS-dependent and LLPS-aboriginal proteins across HeLa (p-value = 1.16 × 10^-7), HEK 293 T (p-value = 2.58 × 10^-9), and SH-SY5Y (p-value = 9.37 × 10^-19) cell lines. The scatter plot illustrates (**f**) the ratio of Low Complexity (LC) domains to the total sequence length in LLPS-dependent and LLPS-aboriginal proteins across HeLa (p-value = 6.11 × 10^-15), HEK 293 T (p-value = 6.96 × 10^-8), and SH-SY5Y (p-value = 0.0076) cell lines. The background group consists of 300 randomly selected proteins from the human proteome. The solid line represents the median, and the dashed line represents the mean. (****: $p < 0.0001$, *: $p < 0.05$). Statistical analysis used a two-tailed unpaired t test. **g** The image shows a comparison between proteins identified by CLAPM in neurodegenerative disease cell models and publicly available databases of LLPS proteins. Source data are provided as a Source Data file.

selected for this experiment. The mouse model employed in this study comprises male mice aged 4 months, assigned to the experimental group, and an additional four wild-type mice as the control group. All animals underwent neurodegenerative disease-related behavioral verification before the experiments. Mice were housed under a specific-pathogen-free (SPF) facility. For organ and tissue collection, phosphate-buffered saline (PBS) cardiac perfusion after anesthesia to remove blood. All samples were placed in liquid nitrogen as soon as possible after stripping and stored at − 80 °C until protein extraction.

Cell culture

HeLa, HEK 293 T, and SH-SY5Y cells were amplified from the early stock of cells purchased from the cell bank of the China Center for Type Culture Collection (CCTCC)

HeLa and HEK 293 T cells were cultured in Dulbecco's Modified Eagle Medium (DMEM) supplemented with 10% fetal bovine serum and 1% penicillin-streptomycin. SH-SY5Y cells were cultured in 44.5% MEM medium and 44.5% Ham's F-12 medium supplemented with 10% fetal bovine serum and 1% penicillin-streptomycin. Cells were incubated in a humid atmosphere at 37 °C, containing 5% CO_2.

For the SILAC experiment, DMEM without L-arginine and L-lysine was supplemented with 10% dialyzed FBS, penicillin/streptomycin, and unlabeled L-lysine: HCL and L-arginine: HCL at 0.4 mM and 0.8 mM, or isotopes labeled L-lysine: 2HCl (13C6, 15N2) and L-arginine: HCL (13C6, 15N4). 200 mg/ml L-proline was added to both heavy and light media.

Lentivirus production and infection

HEK 293 T cells were co-transfected with expression construct pGenLenti-FUS-APEX2-EGFP, pGenLenti--FUS_{P525L}-APEX2-EGFP, pGenLenti-G3BP1-APEX2-EGFP, pGenLenti-TIA1-APEX2-EGFP, and pGenLenti-APEX2-EGFP (untargeted control), along with pMD2.G and psPAX2, and growth media were replaced after 6 h. After 48 hours of transfection, the culture medium containing the virus was harvested, and passed 0.45 μm Filter, concentrate, divide evenly, and quickly freeze through an M-filter. Transduction of wild-type HEK 293 T and 25 at 50% confluence μ L suspension of lentivirus particles, then treated with 4 ng/ml puromycin for 3 days. Harvest cells and verify stable transgenic expression through protein blotting.

Proximity labeling in living cells

Cells were seeded in 10 cm culture dishes the day before labeling. The following day, when they reached approximately 80% confluence, they were either left untreated as a control or treated with 500 μM sodium arsenite for 1 hour at 37 °C to induce stress. During stress induction, 500 μM biotin-phenol (BP) was added to the culture medium simultaneously. For the negative control, exogenous biotin was omitted. Biotinylation was initiated by adding 1 mM hydrogen peroxide for 60 s, followed by quenching the biotinylation reaction with 5 mM Trolox and 10 mM sodium L-ascorbate. The samples were washed three times with cold PBS buffer, cells were harvested using a cell scraper, and the collected pellet was obtained by centrifugation at 1000 × g for 5 min. Suspend the cells in 1 mL of RIPA lysis buffer and incubate at 4 °C for 30 min, followed by sonication for 3 min. Clarify the lysate by centrifugation at 12,500 × g for 4 minutes at 4 °C.

Western blot analysis

Transfected cells and magnetic bead-enriched samples were lysed by the RIPA buffer containing 1% phosphatase (20109ES05, Yeasen, China) and protease inhibitors (20124ES03, Yeasen, China) to extract proteins. The denatured proteins were introduced into an SDS-polyacrylamide gel and subjected to electrophoresis, when the bromophenol blue (BPB) dye migrated to the bottom of the gel. The gel was transferred onto a 0.45 mm polyvinylidene fluoride (PVDF) membrane(Millipore, Germany) pre-stimulated with methanol. The PVDF membrane was blocked by 5% skim milk containing 0.1% Tween-20 (TBST) TBS, then incubated with the corresponding primary antibodies of 1:1000 overnight at 4 °C. The ECL Western Blot Detection System (180 501, Tanon) was used for signal detection after incubation with HRP-conjugated secondary antibodies (33101ES60, Yeasen) at 1:5000 in room temperature for 2 h. A Chemidoc MP imaging system was used to visualize protein expression, and ImageJ software was used to quantify the signals.

The primary antibodies used in this study include anti FLAG labeled rabbit monoclonal antibodies, anti FUS rabbit monoclonal antibodies, and anti EGFP rabbit monoclonal antibodies. These antibodies were used in 5% skim milk of TBST at a dilution of 1:1000. The secondary antibodies used in this study include 1:5000 diluted anti rabbit IgG and anti-mouse IgG.

Fluorescent Imaging for LLPS

Samples were loaded onto a glass slide with a coverslip, and images were acquired on an LSM 800 Basic Operation microscope by ZEISS. Cells fixed in 4% paraformaldehyde for 10 minutes, and then permeate with 10.0% Triton, 5 × PBS for 1 min. Rinse cells with 1 × PBS and block with blocking buffer (1 × PBS, 2% BSA, 0.02% Triton). Incubate with fluorescent dye for 30 min, and wash again. Store cells in darkness at 4 °C or 50% glycerol/PBS for long-term storage.

LLPS experiments under different conditions

For heat shock treatment, the cell culture media was replaced with fresh media prewarmed to 42 °C and placed at 42 °C for 1 h. In recovery experiments, the cells were returned to the 37 °C incubator for the indicated time. For osmotic stress, the media was replaced with fresh media containing 0.4 M sorbitol for 0.5 h. For UV stress, the media was removed and replaced with phosphate-buffered saline (PBS), and 40 J/m^2 UV radiation was delivered.

qRT-PCR analysis

Total RNA from the brain tissues of 50 mg wild mice and diseased mice was extracted by the Trizol-based method, and total RNA was utilized for reverse transcription. Follow the manufacturer's instructions to establish a qPCR reaction using the Hifair One Step RT qPCR SYBR

Green kit. The ΔΔCt method for qPCR analysis involves calculating ΔCt by subtracting the Ct value of the reference gene from the Ct value of the target gene, followed by determining ΔΔCt by subtracting the ΔCt of the control group from the ΔCt of the experimental group, and finally computing relative expression as $2^{-\Delta\Delta Ct}$ to normalize target gene expression to a reference gene (GAPDH) and quantify fold changes relative to a control. For each mRNA expression level in each brain region, two parallel groups were set and averaged. The prime sequence is shown in Supplementary Table S1.

Protein interaction network analysis

Protein interaction data come from the publicly available string website [https://www.string-db.org/]. We used Cytoscape to visualize the PPI dataset, and the internal Cytoscape network analyzer plugin was used to calculate and visualize network parameters.

Protein domain and gene ontology analysis

Domain analysis was done by retrieving PFAM domains through the NCBI Conserved Domains Database [https://www.ncbi.nlm.nih.gov/guide/domains-structures/]. Gene ontology (GO) terms, functional enrichment analysis, and annotation were performed using the web-based tool DAVID and Metascape [http://metascape.org].

Homogenization and digestion

A total of 80 brain tissue samples, derived from 10 distinct brain regions of 8 mice, were rapidly frozen in liquid nitrogen and homogenized by grinding for 40 seconds. Subsequently, lysis buffer containing protease inhibitors was added to the tissues, followed by sonication for 10 minutes. After centrifugation at 10,000 × *g* for 20 min, the supernatant was collected for protein quantification and stored for further analysis.

72 cell samples from 3 cell lines under 8 treatment conditions ($n = 3$) were subjected to proximity labeling experiments and magnetic bead enrichment. The magnetic beads were washed twice with 100 µL of RIPA buffer and then incubated with approximately 10 mg of cell lysate at room temperature with shaking for 2 h. Subsequently, the beads were washed once with 1 mL of RIPA lysis buffer and then twice with 1 mL of 8 M urea. After washing, they were centrifuged at low speed for 5 min. The supernatant was removed. The 100 µL of 50 mM ammonium bicarbonate buffer was added for protein quantification and stored for further analysis.

For digestion, a total of 100 µg protein per sample was precipitated in acetone overnight at − 20 °C. The protein pellet was obtained after centrifugation at 14,000 × *g* for 20 min, and the pellet was washed twice with acetone. After discarding the supernatant and evaporating the residual acetone, the pellet was resuspended in 7 M guanidine hydrochloride. The protein solution was reduced with 10 mM dithiothreitol (DTT) at 55 °C for 1 h and alkylated by 20 mM iodoacetamide (IAA) for 30 min in the dark. Samples were washed with ammonium bicarbonate on 10 kDa ultrafiltration concentrators (Sartorius) to purify the protein. Finally, the trypsin (Promega) digestion was performed overnight at 37 °C using a 50:1 protein: protease ratio (w/w). After termination of digestion by the addition of a final concentration of 1% formic acid (FA), the peptides were desalted using a C18 spin column (Monospin) according to the manufacturer's instructions. Peptides eluted were dried under vacuum and stored at − 80 °C until subsequent use for liquid chromatography tandem mass spectrometry (LC-MS/MS) analysis.

LC-MS/MS Analysis

Reverse phase chromatography was performed with an EASY-nLC 1200 system (Thermo Fisher Scientific), which was coupled to an Orbitrap mass spectrometer (Q Exactive HF-X, Thermo Fisher Scientific). Samples were dissolved at 0.5 µg/µl spiked with iRT (Biognosys), and 1 µl of each sample was loaded onto 2 cm × 75 µm homemade reversed-phase C18 column (particle size, 3 µm; pore size, 100 Å. Thermo Fisher Scientific) and separated by 25 cm × 75 µm analytical column (particle size, 2 µm; pore size, 100 Å. Thermo Fisher Scientific). Separation was performed over a 120 min gradient at a flow rate of 300 nl/min. 0-1 min with buffer B ranging from 1% to 8%; 1–81 min with buffer B ranging from 8% to 22%; 81–98 min with buffer B ranging from 22% to 28%; 98–112 min with buffer B ranging from 28% to 36%; 112–116 min with buffer B ranging from 36% to 100%; 116–120 min with buffer B 100%. (buffer A: 0.1% FA; buffer B: 0.1% FA in 80% CAN). MS data were acquired with a shotgun proteomics method, where in each cycle, a full scan was acquired at a resolution of 60,000 with a mass range of 350–1800 m/z. Up to 20 most intense precursor ions with charge ≥ 2 were selected with an isolation window of 1.6 Da and subsequently fragmented by higher-energy collisional dissociation (HCD) with a normalized collision energy of 28%. The MS/MS scans were acquired at a resolution of 15000. The precursor ions were dynamically excluded from reselection for 60 s. Trypsin digests of Hela cells as quality control samples were assayed before each organ cohort started and after routine equipment calibration to ensure instrument condition. All sample mixture was assayed every 8 LC-MS/MS injections as a control to ensure good sensitivity and reproducibility.

Protein identification and quantification

Proteome database searched for raw files from [https://www.uniprot.org/] Universal Protein Resources (UniProt). The PD search strategy was as follows. Protein identification required at least one unique peptide with a minimum length of 6 amino acids. The maximum value of trypsin leakage was 2. The error detection rate (FDR) of the filter was less than 1% for filtering peptides and peptide spectral matching, as well as peptides. Specifically, the search included variable modifications of N-terminal methionine excision and cystine aminoformyl methylation; The length of the peptide ranges from 7 to 30, and the precursor FDR was stewed for 1.0%. Due to abnormal mass spectrometry data collection, one brain sample was taken out at one week, and 299 mass spectra were used for data analysis.

Quantification and statistical analyses

Perform bioinformatics analysis using Perseus software (v1.6.15.0), R (v4.2.0), Origin (v2022b), and the Wu Kong platform. Before further analysis, the impact related to the batch was eliminated from the data. The sample effect is estimated based on PG with an effective value exceeding 70% to avoid bias due to missing values. After filtering the effective values, we calculate the median normalized abundance through log2 transfer values. After imputation of missing values, perform unsupervised clustering t-SNE. In the case of FDR < 0.05, the differential expression of PGs in the group was calculated using the ANOVA test using the Benjamin Hochberg program. After filtering rows in the PGs matrix based on at least one set of valid values exceeding 70% (5 biological replicates per gender at each time point). Calculate Pearson correlation coefficient for inter-experimental correlation analysis. For paired comparisons of each organ at different age points, Student *t* test (double tailed) was used to analyze the data between two time points after missing value filtering, interpolation, and coefficient variation filtering, and only statistically significant genes ($\log_2$ (multiple change) truncation value > 1.0) were analyzed; Benjamin Hochberg adjusted $p < 0.05$ to include in downstream analysis. Statistical significance is represented in all figures, as follows: *p*-value of < 0.0001: ****, *p*-value of 0.0001 to 0.001: ***, *p*-value of 0.001 to 0.01: **, *p*-value of 0.01 to 0.05: * and *p*-value of ≥ 0.05: not significant.

Statistics and reproducibility

In addition to the sample sizes, exclusion criteria, and statistics discussed in the rest of the Methods section, more information can also be found in the Reporting summary. In this study, the confocal

micrographs presented in Figs. 2b, c, 3d, and 5a are representative images derived from experiments independently replicated three times. The in vitro droplet aggregation assay depicted in Fig. 2a was conducted with five independent experimental replicates. Each replication yielded analogous results, confirming the consistency and reproducibility of the observed phenomena.

Reporting summary

Further information on research design is available in the Nature Portfolio Reporting Summary linked to this article.

Data availability

The mass spectrometry proteomics data generated in this study have been deposited in the ProteomeXchange Consortium via the PRIDE partner repository database under accession code PXD051405. Information on mass spectrometry file organization can be found in Supplementary Note 1. Unless otherwise stated, all data supporting the results of this study can be found in the article, supplementary, and source data files. Source data are provided in this paper.

References

1. Su, X. et al. Phase separation of signaling molecules promotes T cell receptor signal transduction. *Science* **352**, 595–599 (2016).
2. Du, M. & Chen, Z. J. DNA-induced liquid phase condensation of cGAS activates innate immune signaling. *Science* **361**, 704–709 (2018).
3. Sabari, B. R. et al. Coactivator condensation at super-enhancers links phase separation and gene control. *Science* **361**, https://doi.org/10.1126/science.aar3958 (2018).
4. Strom, A. R. et al. Phase separation drives heterochromatin domain formation. *Nature* **547**, 241–245 (2017).
5. Larson, A. G. et al. Liquid droplet formation by HP1alpha suggests a role for phase separation in heterochromatin. *Nature* **547**, 236–240 (2017).
6. Molliex, A. et al. Phase separation by low complexity domains promotes stress granule assembly and drives pathological fibrillization. *Cell* **163**, 123–133 (2015).
7. Zhang, G., Wang, Z., Du, Z. & Zhang, H. mTOR Regulates phase separation of PGL granules to modulate their autophagic degradation. *Cell* **174**, 1492–1506 (2018).
8. Sun, D., Wu, R., Zheng, J., Li, P. & Yu, L. Polyubiquitin chain-induced p62 phase separation drives autophagic cargo segregation. *Cell Res.* **28**, 405–415 (2018).
9. Milovanovic, D., Wu, Y., Bian, X. & De Camilli, P. A liquid phase of synapsin and lipid vesicles. *Science* **361**, 604–607 (2018).
10. Yoshizawa, T. et al. Nuclear import receptor inhibits phase separation of FUS through binding to multiple sites. *Cell* **173**, 693–705 (2018).
11. Nozawa, R. S. et al. Nuclear microenvironment in cancer: Control through liquid-liquid phase separation. *Cancer Sci.* **111**, 3155–3163 (2020).
12. Hofweber, M. et al. Phase separation of FUS is suppressed by its nuclear import receptor and arginine methylation. *Cell* **173**, 706–719 (2018).
13. Guo, L. et al. Nuclear-import receptors reverse aberrant phase transitions of RNA-binding proteins with prion-like domains. *Cell* **173**, 677–692 (2018).
14. Li, P. et al. Phase transitions in the assembly of multivalent signalling proteins. *Nature* **483**, 336–340 (2012).
15. Wang, J. et al. A molecular grammar governing the driving forces for phase separation of prion-like RNA binding proteins. *Cell* **174**, 688–699 (2018).
16. Yu, C. et al. Distinctive network topology of phase-separated proteins in human interactome. *J. Mol. Biol.* **434**, 167292 (2022).
17. Mondal, S. et al. Multivalent interactions between molecular components involved in fast endophilin mediated endocytosis drive protein phase separation. *Nat. Commun.* **13**, 5017 (2022).
18. Gracia, P. et al. Molecular mechanism for the synchronized electrostatic coacervation and co-aggregation of alpha-synuclein and tau. *Nat. Commun.* **13**, 4586 (2022).
19. Ferrolino, M. C., Mitrea, D. M., Michael, J. R. & Kriwacki, R. W. Compositional adaptability in NPM1-SURF6 scaffolding networks enabled by dynamic switching of phase separation mechanisms. *Nat. Commun.* **9**, 5064 (2018).
20. Day, K. J. et al. Liquid-like protein interactions catalyse assembly of endocytic vesicles. *Nat. Cell Biol.* **23**, 366–376 (2021).
21. Ray, S. et al. alpha-Synuclein aggregation nucleates through liquid-liquid phase separation. *Nat. Chem.* **12**, 705–716 (2020).
22. Ambadipudi, S., Biernat, J., Riedel, D., Mandelkow, E. & Zweckstetter, M. Liquid-liquid phase separation of the microtubule-binding repeats of the Alzheimer-related protein Tau. *Nat. Commun.* **8**, 275 (2017).
23. Schmidt, H. B., Barreau, A. & Rohatgi, R. Phase separation-deficient TDP43 remains functional in splicing. *Nat. Commun.* **10**, 4890 (2019).
24. Patel, A. et al. A liquid-to-solid phase transition of the ALS protein FUS accelerated by disease mutation. *Cell* **162**, 1066–1077 (2015).
25. Polymenidou, M. & Cleveland, DonW. The seeds of neurodegeneration: Prion-like spreading in ALS. *Cell* **147**, 498–508 (2011).
26. Ambadipudi, S., Biernat, J., Riedel, D., Mandelkow, E. & Zweckstetter, M. Liquid–liquid phase separation of the microtubule-binding repeats of the Alzheimer-related protein Tau. *Nat. Commun.* **8**, 275 (2017).
27. Alberti, S., Gladfelter, A. & Mittag, T. Considerations and challenges in studying liquid-liquid phase separation and biomolecular condensates. *Cell* **176**, 419–434 (2019).
28. Jain, S. et al. ATPase-Modulated stress granules contain a diverse proteome and substructure. *Cell* **164**, 487–498 (2016).
29. Hubstenberger, A. et al. P-Body purification reveals the condensation of repressed mRNA regulons. *Mol. Cell* **68**, 144–157 (2017).
30. Burke, K. A., Janke, A. M., Rhine, C. L. & Fawzi, N. L. Residue-by-residue view of in vitro FUS granules that bind the C-terminal domain of RNA polymerase II. *Mol. Cell* **60**, 231–241 (2015).
31. Mitrea, D. M. et al. Self-interaction of NPM1 modulates multiple mechanisms of liquid–liquid phase separation. *Nat. Commun.* **9**, 842 (2018).
32. Shin, Y. et al. Spatiotemporal control of intracellular phase transitions using light-activated optoDroplets. *Cell* **168**, 159–171 (2017).
33. Youn, J.-Y. et al. High-density proximity mapping reveals the subcellular organization of mRNA-associated granules and bodies. *Mol. Cell* **69**, 517–532 (2018).
34. Kwak, C. et al. Identification of proteomic landscape of drug-binding proteins in live cells by proximity-dependent target ID. *Cell Chem. Biol.* **29**, 1739–1753 (2022).
35. Na, Z. et al. Mapping subcellular localizations of unannotated microproteins and alternative proteins with MicroID. *Mol. Cell* **82**, 2900–2911 (2022).
36. Markmiller, S. et al. Context-dependent and disease-specific diversity in protein interactions within stress granules. *Cell* **172**, 590–604 (2018).
37. Liu, Z. et al. Hsp27 chaperones FUS phase separation under the modulation of stress-induced phosphorylation. *Nat. Struct. Mol. Biol.* **27**, 363–372 (2020).
38. Murray, D. T. et al. Structure of FUS protein fibrils and its relevance to self-assembly and phase separation of low-complexity domains. *Cell* **171**, 615–627 (2017).
39. Lam, S. S. et al. Directed evolution of APEX2 for electron microscopy and proximity labeling. *Nat. Methods* **12**, 51–54 (2015).
40. Hoheisel, J. et al. Empirical bayes analysis of quantitative proteomics experiments. *PLoS ONE* **4**, https://doi.org/10.1371/journal.pone.0007454 (2009).
41. Kammers, K., Cole, R. N., Tiengwe, C. & Ruczinski, I. Detecting significant changes in protein abundance. *EuPA Open Proteom.* **7**, 11–19 (2015).

42. Bussi, C. et al. Stress granules plug and stabilize damaged endolysosomal membranes. *Nature* **623**, 1062–1069 (2023).
43. Maxwell, B. A. et al. Ubiquitination is essential for recovery of cellular activities after heat shock. *Science* **372**, https://doi.org/10.1126/science.abc3593 (2021).
44. Cui, Q., Liu, Z. & Bai, G. Friend or foe: The role of stress granule in neurodegenerative disease. *Neuron* **112**, 2464–2485 (2024).
45. Youn, J.-Y. et al. Properties of stress granule and P-body proteomes. *Mol. Cell* **76**, 286–294 (2019).
46. Uversky, V. N. Intrinsically disordered proteins in overcrowded milieu: Membrane-less organelles, phase separation, and intrinsic disorder. *Curr. Opin. Struct. Biol.* **44**, 18–30 (2017).
47. Yasuda, S. et al. Stress- and ubiquitylation-dependent phase separation of the proteasome. *Nature* **578**, 296–300 (2020).
48. Sheng, X., Xia, Z., Yang, H. & Hu, R. The ubiquitin codes in cellular stress responses. *Protein Cell* **15**, 157–190 (2023).
49. Otten, E. G. et al. Ubiquitylation of lipopolysaccharide by RNF213 during bacterial infection. *Nature* **594**, 111–116 (2021).
50. Liu, Q. et al. RNA-binding protein hnRNPR reduces neuronal cholesterol levels by binding to and suppressing HMGCR. *J. Integr. Neurosci.* **20**, 265–276 (2021).
51. Kim, Y. K. et al. hCLE/C14orf166 Associates with DDX1-HSPC117-FAM98B in a novel transcription-dependent shuttling RNA-transporting complex. *PLoS ONE* **9**, https://doi.org/10.1371/journal.pone.0090957 (2014).
52. Lee, Y.-J., Wei, H.-M., Chen, L.-Y. & Li, C. Localization of SERBP1 in stress granules and nucleoli. *FEBS J.* **281**, 352–364 (2014).
53. Li, Y. R., King, O. D., Shorter, J. & Gitler, A. D. Stress granules as crucibles of ALS pathogenesis. *J. Cell Biol.* **201**, 361–372 (2013).
54. Dawson, T. M., Golde, T. E. & Lagier-Tourenne, C. Animal models of neurodegenerative diseases. *Nat. Neurosci.* **21**, 1370–1379 (2018).
55. Mead, R. J., Shan, N., Reiser, H. J., Marshall, F. & Shaw, P. J. Amyotrophic lateral sclerosis: a neurodegenerative disorder poised for successful therapeutic translation. *Nat. Rev. Drug Discov.* **22**, 185–212 (2022).
56. Chen, H. et al. Activation of Pgk1 results in reduced protein aggregation in diverse neurodegenerative conditions. *Mol. Neurobiol.* **60**, 5090–5101 (2023).
57. Domi, T. et al. Unveiling the SOD1-mediated ALS phenotype: insights from a comprehensive meta-analysis. *J. Neurol.* **271**, 1342–1354 (2023).
58. Pinares-Garcia, P., Stratikopoulos, M., Zagato, A., Loke, H. & Lee, J. Sex: A significant risk factor for neurodevelopmental and neurodegenerative disorders. *Brain Sci.* **8**, https://doi.org/10.3390/brainsci8080154 (2018).
59. Ullah, M. F. et al. Impact of sex differences and gender specificity on behavioral characteristics and pathophysiology of neurodegenerative disorders. *Neurosci. Biobehav. Rev.* **102**, 95–105 (2019).
60. Bettegazzi, B. et al. Casein Kinase 2 dependent phosphorylation of eIF4B regulates BACE1 expression in Alzheimer's disease. *Cell Death Dis.* **12**, 769 (2021).
61. Laut, A. K. et al. CHD5 inhibits metastasis of neuroblastoma. *Oncogene* **41**, 622–633 (2022).
62. Guenther, U.-P. et al. Clinical variability in distal spinal muscular atrophy type 1 (DSMA1): determination of steady-state IGHMBP2 protein levels in five patients with infantile and juvenile disease. *J. Mol. Med.* **87**, 31–41 (2008).
63. Zheng, K. et al. HSV-1-encoded microRNA miR-H1 targets Ubr1 to promote accumulation of neurodegeneration-associated protein. *Virus Genes* **54**, 343–350 (2018).
64. Guenther, U.-P. et al. IGHMBP2 is a ribosome-associated helicase inactive in the neuromuscular disorder distal SMA type 1 (DSMA1). *Hum. Mol. Genet.* **18**, 1288–1300 (2009).
65. Rzepnikowska, W. & Kochański, A. Models for IGHMBP2-associated diseases: an overview and a roadmap for the future. *Neuromuscul. Disord.* **31**, 1266–1278 (2021).
66. Schottmann, G. et al. Recessive truncating IGHMBP2 mutations presenting as axonal sensorimotor neuropathy. *Neurology* **84**, 523–531 (2015).
67. Shababi, M. et al. Rescue of a mouse model of spinal muscular atrophy with respiratory distress type 1 by AAV9-IGHMBP2 is dose dependent. *Mol. Ther.* **24**, 855–866 (2016).

Acknowledgements

This work was supported by National Key R&D Program of China (2022YFC2601700, 2022YFF0710202) and NSFC Projects (T2122002, 22077079, 81871448), Shanghai Municipal Science and Technology Project(22Z510202478), Shanghai Municipal Education Commission Project(21SG10), Shanghai Jiao Tong University Projects (YG2021ZD19, 2020 SJTU-HUJI), Shanghai Municipal Health Commission Project (2019CXJQ03) to X.D. Thanks for AEMD SJTU, Shanghai Jiao Tong University Laboratory Animal Center for the supporting.

Author contributions

S.S. designed the study and performed most of the experiments. S.S. wrote the original draft. H.X., L.J., and X.D. edited the manuscript. Q.W. and Y.Z. performed the mouse sample collection. J.X. performed the confocal photography. X.S. performed the Western blot. S.S. and R.C. assisted in the data analysis.

Competing interests

The authors declare no competing interests.

Additional information

Supplementary information The online version contains supplementary material available at https://doi.org/10.1038/s41467-025-59457-z.

Correspondence and requests for materials should be addressed to Xianting Ding.

Peer review information *Nature Communications* thanks the anonymous reviewers for their contribution to the peer review of this work. A peer review file is available.